



Large-area waterproof and durable perovskite luminescent textiles

Received: 29 July 2022

Accepted: 2 January 2023

Published online: 16 January 2023

Check for updates

Tian Tian^{1,4}, Meifang Yang^{1,4}, Yuxuan Fang¹, Shuo Zhang¹, Yuxin Chen², Lianzhou Wang³ & Wu-Qiang Wu¹

Lead halide perovskites show great potential to be used in wearable optoelectronics. However, obstacles for real applications lie in their instability under light, moisture and temperature stress, noxious lead ions leakage and difficulties in fabricating uniform luminescent textiles at large scale and high production rates. Overcoming these obstacles, we report simple, high-throughput electrospinning of large-area ($> 375 \text{ cm}^2$) flexible perovskite luminescent textiles woven by ultra-stable polymer@perovskite@cyclodextrin@silane composite fibers. These textiles exhibit bright and narrow-band photoluminescence (a photoluminescence quantum yield of 49.7%, full-width at half-maximum $< 17 \text{ nm}$) and the time to reach 50% photoluminescence of 14,193 h under ambient conditions, showcasing good stability against water immersion ($> 3300 \text{ h}$), ultraviolet irradiation, high temperatures (up to 250 °C) and pressure surge (up to 30 MPa). The waterproof PLTs withstood fierce water scouring without any detectable leaching of lead ions. These low-cost and scalable woven PLTs enable breakthrough application in marine rescue.

Lead halide perovskites (LHPs) form a new generation of luminescent materials owing to their fascinating optoelectronic properties such as tunable bandgaps, high color purity and high photoluminescence quantum yield (PLQY)^{1–13}. These properties enable a myriad of optoelectronic applications, such as lighting and displays, making a huge impact and challenging conventional light-emitting technologies and devices^{10–13}. Despite recent advances in optoelectronic performances, the inherent imperfections and instability have been big obstacles to the practical application of LHPs devices. LHPs must overcome the decomposition upon exposure to light, heat and moisture. Encapsulating LHPs within polymers, metal oxides, nanosilica, porous alumina membranes, or making LHP-glass nanocomposites have been variously developed to stabilize the LHPs and impart advanced photonic functionalities^{14–24}. However, these approaches entail several complicated synthetic (e.g. tailoring of chemical composition, bandgap and ligand anchoring of LHPs)^{25–27} and processing (e.g. supporting mesoporous template preparation, sol-gel preparation, coating, sintering or

laser lithography) steps^{28–34}. Due to the fast crystallization of LHPs, it is challenging to produce uniform perovskite thin films on a large scale by the common mass-fabrication techniques. In recent years, not only being integrated on small-area rigid panels, the state-of-the-art LHP-based light-emitting thin films or devices are also assembled into large-area, flexible and/or wearable electronics^{35–40}. In particular, the electrospinning technique has been demonstrated as one of the most ideal ways to fabricate perovskite luminescent fibrous membranes^{35–38}. Unfortunately, the current methodologies were limited to stabilizing the LHPs within a chosen polymer matrix featuring less functional groups, which then exhibited poor mechanical stability caused by weak interfacial interactions. In this case, the perovskite is only partially protected and its surface defects are not well-passivated, thus showing inferior PLQY and moderate stability against water invasion and UV irradiation. Nonetheless, through rational interfacial engineering by purposely designed chemical interactions to stabilize the LHP and mitigate the leaching of toxic heavy metal ions, we envision

¹MOE Key Laboratory of Bioinorganic and Synthetic Chemistry, Lehn Institute of Functional Materials, School of Chemistry, Sun Yat-sen University, Guangzhou 510006, P. R. China. ²Instrumental Analysis and Research Center, Sun Yat-sen University, Guangzhou 510275, P. R. China. ³Nanomaterials Centre, School of Chemical Engineering and Australian Institute for Bioengineering and Nanotechnology, The University of Queensland, Brisbane, QLD 4072, Australia. ⁴These authors contributed equally: Tian Tian, Meifang Yang. e-mail: l.wang@uq.edu.au; wuwq36@mail.sysu.edu.cn

that perovskite luminescent fibers can be woven into textiles for smart wearable optoelectronics.

We present a simple, single-nozzle electrospinning method that can directly and continuously fabricate PLTs on a large-scale with high production rates of $\sim 1500 \text{ cm}^2 \text{ h}^{-1}$. Significantly distinguished to the previous works regarding polymer-encapsulated perovskite composites^{35–38}, a new class of composited fibers with perovskites robustly encapsulated in polymers, cyclodextrin supermolecules and fluorinated hydrophobic agents was designed. Similar to other reports, the polymer acts as a fibrous matrix for loading perovskites and ensures mechanical flexibility. Beyond that, we innovatively introduced cyclodextrin supermolecules, which feature multidentate hydroxyl groups along the walls of internal and external cavities, and can strongly interact with perovskites to form a stable host-guest complex that simultaneously passivates the crystallographic imperfections in the perovskites. In the meantime, the super-hydrophobic fluorine-containing silane was incorporated, which forms strong hydrogen bonds with the cyclodextrin molecules, further strengthening the stabilization effect and providing a robust physical barrier at the outer surface against moisture invasion. The woven luminescent textiles showed great flexibility, stability and prominent optical properties (i.e. high PLQY, high color purity and uniform emission), and hence their potential application in a wide variety of flexible, wearable optoelectronics were demonstrated. We show that the combination of strategies of host-guest inclusion, multidentate interaction and multiple passivation by cyclodextrin molecules, as well as in-situ encapsulation and outer-layer physical barrier protection by fluorine-containing silanes enable the PLTs to be very stable against long-term water immersion ($>3300 \text{ h}$, regardless of pH), high power ultraviolet light irradiation (UV; wavelength of 365 nm, a power density

of 120 mW cm^{-2}), high temperatures up to 250°C , or high pressures up to 30 MPa. Up till now, none of the currently reported works regarding polymer-encapsulated perovskite composites have addressed the toxic Pb leakage issue, which would limit their practical application of perovskite-based textiles. Encouragingly, our demonstrated new composited structure ideally addressed the Pb leakage issue, with only $\sim 3.94 \text{ ppt}$ of Pb^{2+} ions leaching out even after dynamic water scouring of PLTs for $>3300 \text{ h}$, making the PLTs environmentally viable and safe. To the best of our knowledge, our demonstrated PLTs represented one of the most promising overall performances in terms of luminescent properties (PLQYs, narrow FWHM), stability against water/heat/pressure, scalability, cost advantage and safety, etc.

Results

Composites synthesis and chemical interaction analysis

$\text{CsPbBr}_3@\text{hydroxypropyl-}\beta\text{-cyclodextrin (HP}\beta\text{CD)}$ composites were first synthesized mechanochemically by grinding. The HP β CD molecule has distinct structural features in terms of its hydrophobic inner cavity (ca. 0.78 nm in diameter, Supplementary Fig. 1)^{41,42}, which can be used as host matrices for forming host-guest composites, such as $\text{CsBr}@\text{HP}\beta\text{CD}$ and $\text{PbBr}_2@\text{HP}\beta\text{CD}$. During continuous grinding, we expected that $\text{CsBr}@\text{HP}\beta\text{CD}$ and $\text{PbBr}_2@\text{HP}\beta\text{CD}$ composites could completely react to form $\text{CsPbBr}_3@\text{HP}\beta\text{CD}$ composites. In this case, the HP β CD would self-aggregate and copolymerize to form a network of clusters with mesoscale and/or macroscale cavities, which can spatially limit the crystal growth and confine the particle sizes of the evolved CsPbBr_3 nanocrystals. The HP β CD clusters were spontaneously extruded out to the surface of the CsPbBr_3 nanocrystal to form an ingenious stable host-guest complex, which simultaneously stabilized and passivated the surface states of CsPbBr_3 . Grinding CsBr ,

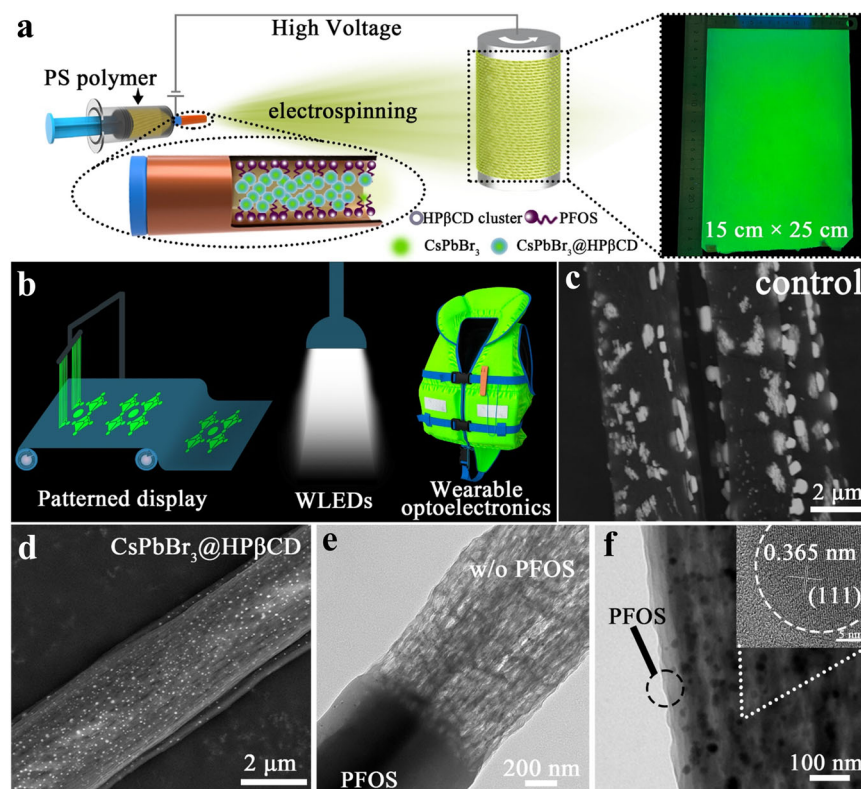


Fig. 1 | Schematic illustration of the fabrication process of PLTs and morphological characterization. **a** Schematic illustration of the fabrication process of PLTs and the as-prepared fibrous membrane under UV light irradiation. **b** Application of $\text{CsPbBr}_3@\text{HP}\beta\text{CD}@\text{PFOS}$ composites in patterned display, white light-emitting diodes (WLEDs) and wearable optoelectronics. SEM (YAG back-scattered electron

detector) images of the **(c)** control fiber and **(d)** $\text{CsPbBr}_3@\text{HP}\beta\text{CD}$ fiber. **e** TEM image showing the $\text{CsPbBr}_3@\text{HP}\beta\text{CD}$ fiber without or with PFOS coating as indicated. Note: the top half of the $\text{CsPbBr}_3@\text{HP}\beta\text{CD}@\text{PFOS}$ fiber was selectively etched by n-hexane to expose the inner $\text{CsPbBr}_3@\text{HP}\beta\text{CD}$. **f** Close-up TEM image of the $\text{CsPbBr}_3@\text{HP}\beta\text{CD}@\text{PFOS}$ fiber. Inset: HRTEM image of the CsPbBr_3 crystal.

PbBr₂ and HPβCD blended powder significantly improved the color purity and enhanced the luminescent brightness by more than four-fold, relative to a ground CsBr and PbBr₂ blended powder (Supplementary Fig. 2). X-ray photoelectron spectroscopy (XPS) and Fourier Transform Infrared spectroscopy (FTIR) characterizations were conducted to identify the chemical interaction between HPβCD and CsPbBr₃ and verify the specific passivation function of HPβCD on CsPbBr₃. The XPS results showed the Pb 4f signal peak shifted to higher binding energy upon HPβCD incorporation (Supplementary Fig. 3), suggesting the change of electronic cloud density surrounding Pb²⁺ owing to the strong coordination bonding between electron-donating -OH group in HPβCD and under-coordinated Pb²⁺ ions in perovskites. Such a chemical interaction between Lewis base-typed additives and perovskites has been widely reported⁴³. In addition, we expected that many positively charged hydrogen ions of HPβCD could also strongly interact with negatively charged halide ions in perovskites via electrostatic interaction and/or hydrogen bonding⁴⁴. To further verify the bonding status of H element in HPβCD, the two-dimensional (2D) ¹H-¹H nuclear Overhauser effect spectroscopy (NOESY) cross-peak intensity was measured, which can clearly distinguish between free and bound HPβCD molecules. Free HPβCD molecules behave like small molecules and develop slightly negative or even no nuclear Overhauser effect (NOE) due to a small negative or zero cross-relaxation rate (Supplementary Fig. 4)⁴⁵. However, if HPβCD cluster interacted and was bound to the CsPbBr₃ surface, it will develop large and positive NOEs due to a large and positive cross-relaxation rate^{46,47}. The ¹H NMR of HPβCD was estimated by ChemDraw 19.0 software (Supplementary Fig. 5a). NOESY spectra of CsPbBr₃@HPβCD samples showed many positive cross peaks at ~3.34 ppm (Supplementary Fig. 5b), which indicated a large portion of intramolecular hydrogen bonds forming between HPβCD clusters with multidentate functional groups and CsPbBr₃ perovskites. Overall, the NMR and XPS results synergistically verified the strong interaction between HPβCD molecules/clusters and CsPbBr₃, which is beneficial to effectively passivate the undercoordinated metal cations and stabilize the halide anions (reduce the halide vacancies and/or mitigate their migration) in CsPbBr₃.

Fabrication of large-area PLTs and morphological characterization

The aggregation of CsPbBr₃ nanocrystals (Supplementary Fig. 6a, b) were effectively suppressed in the CsPbBr₃@HPβCD composites, in which the CsPbBr₃ nanocrystals were uniformly encapsulated and spatially isolated by HPβCD clusters (Supplementary Fig. 6c). We identified CsPbBr₃ nanocrystals as the major luminescent source within the composite fragment, and there is a portion of light scattering to the surrounding HPβCD clusters (Supplementary Fig. 6d). Note, it is the most ideal case that the CsPbBr₃ crystal was fully encapsulated in HPβCD cluster. In the real case, there is still some chance that a CsPbBr₃ crystal is half-coated in an HPβCD cluster, in which the sizes of perovskite crystals and/or the cavities of self-formed HPβCD clusters should be carefully controlled. After grinding, we mixed CsPbBr₃@HPβCD powder, polystyrene (PS) and perfluorooctyltriethoxysilane (PFOS) at designed weight ratios in a binary solvent of N,N'-dimethylformamide (DMF) and dimethyl sulfoxide (DMSO) to prepare the electrospinning ink, which was ready to be used for large-area PLTs fabrication via single-nozzle electrospinning (Fig. 1a and Supplementary Fig. 7, see details in the "Methods" section of Supplementary Materials). Note, rather than prior mechanochemical grinding, the electrospinning ink can also be prepared by directly mixing CsBr, PbBr₂, HPβCD, PS and PFOS ingredients together and stirring for 6 h, which then can be directly used to fabricate the large-area PLTs via electrospinning (Supplementary Fig. 8). And the mechanochemical grinding step is intentionally designed to obtain the CsPbBr₃@HPβCD compositized powders and elucidate the beneficial

roles of HPβCD inclusion and passivation on improving the luminescent properties of CsPbBr₃. A 25 cm × 15 cm PLT was produced within 30 min, which had uniform green light emission over the whole display area (Fig. 1a and Supplementary Fig. 9), demonstrating a great potential to be used in large-area patterned displays, flat-panel lighting and other wearable optoelectronics (Fig. 1b). Note, the previously reported electrospinning techniques still require to use 2 or 3 nozzles to load each individual ingredient, such as metal halides, inorganic/organic halide salts and polymers, which is complicated and hard to control the electrospinning parameters and reaction process^{35–38}. In our case, we simply relied on using single-nozzle containing all the ingredients including perovskites, polymers, cyclodextrins and silanes to achieve high-throughput fabrication of high-quality PLTs, which represents a technological advance, especially in terms of reducing fabrication cost and being more compatible to the industrial-scale mass production. Fluorescence confocal microscopy confirmed the fibrous morphology and verified the fluorescence characteristic in the targeted PLT. A consistent, bright fluorescence was detected from individual fibers, inferring the uniform dispersion of effective luminescent perovskite components (Supplementary Fig. 10). An electrospinning process lasting 3 min yielded a similar-sized textile with observable light emission (Supplementary Fig. 11 and Supplementary Movie #1), suggesting the possibility of realizing high-throughput mass production. Indeed, electrospinning is a process of densification, with increased numbers of fibers well-interconnected and woven into a high density but lightweight fibrous network (i.e. ~10–100 mg for a ~375 cm² textile). The electros pinned PLTs also have superior advantages in terms of reduced material cost and simplified fabrication process. To weave a 2.8 m textile (280 cm × 15 cm, Supplementary Fig. 12), only 0.464 g CsPbBr₃ powder, 0.104 g of HPβCD, 1.2 ml of PFOS, 1.22 g of PS and 8 ml of mixed DMF-DMSO solvent were needed. In addition, the PLTs fabrication does not require tedious procedures, such as ligand exchange, solvent washing and high-temperature processing. Overall, the cost of the luminous textile was calculated to be as low as ~0.05 cents cm⁻², demonstrating the prospect of low-cost mass production (Supplementary Table 1).

To elucidate the specific role of the PS polymer, cyclodextrin and silane, we investigated the morphologies of different PLT fibrous membranes. During the electrospinning process, the PS polymer served as a fibrous scaffold holding the CsPbBr₃ nanocrystals within the matrix. However, numerous irregular-shaped CsPbBr₃ crystals were randomly distributed and aggregated on the surface of the fibrous composites (Fig. 1c, Supplementary Fig. 13a, b). In contrast, the fibrous film made from the CsPbBr₃@HPβCD composites showed more uniform dispersion of perovskite nanocrystals with smaller sizes inside and/or at the surface of the polymer matrix (Fig. 1d), which further strengthened the quantum confinement effect and might induce blue-shift of absorption band edge^{14,48}. The CsPbBr₃@HPβCD fibrous films are composed of uniform fibers with hierarchical structures and diameters of several micrometers; each microfiber consists of tiny nanowires with diameters of tens of nanometers (Supplementary Fig. 13c, d). However, the exposure of CsPbBr₃ nanocrystals on the membrane surface is unfavorable for ensuring the good water resistance of the CsPbBr₃@HPβCD fibrous film, thus limiting its practical use and shortening its lifespan. To address this issue, PFOS was incorporated as a separated nanophase ingredient into CsPbBr₃@HPβCD composites during the electrospinning process. On the one hand, PFOS could be spontaneously expelled and fully cover the outer surface of the fibers, so that exposed CsPbBr₃ nanocrystals were not observed (Fig. 1e, Supplementary Fig. 13e, f). On the other hand, the hydrophobic PFOS molecules with many fluorine (F) atoms can form strong hydrogen bonds with the numerous -OH groups in HPβCD, thus constructing a seamless interfacial contact with the CsPbBr₃@HPβCD composite fibers, which, crucially serves as a robust protection layer (~ 50 nm in thickness, Fig. 1f) to enhance the

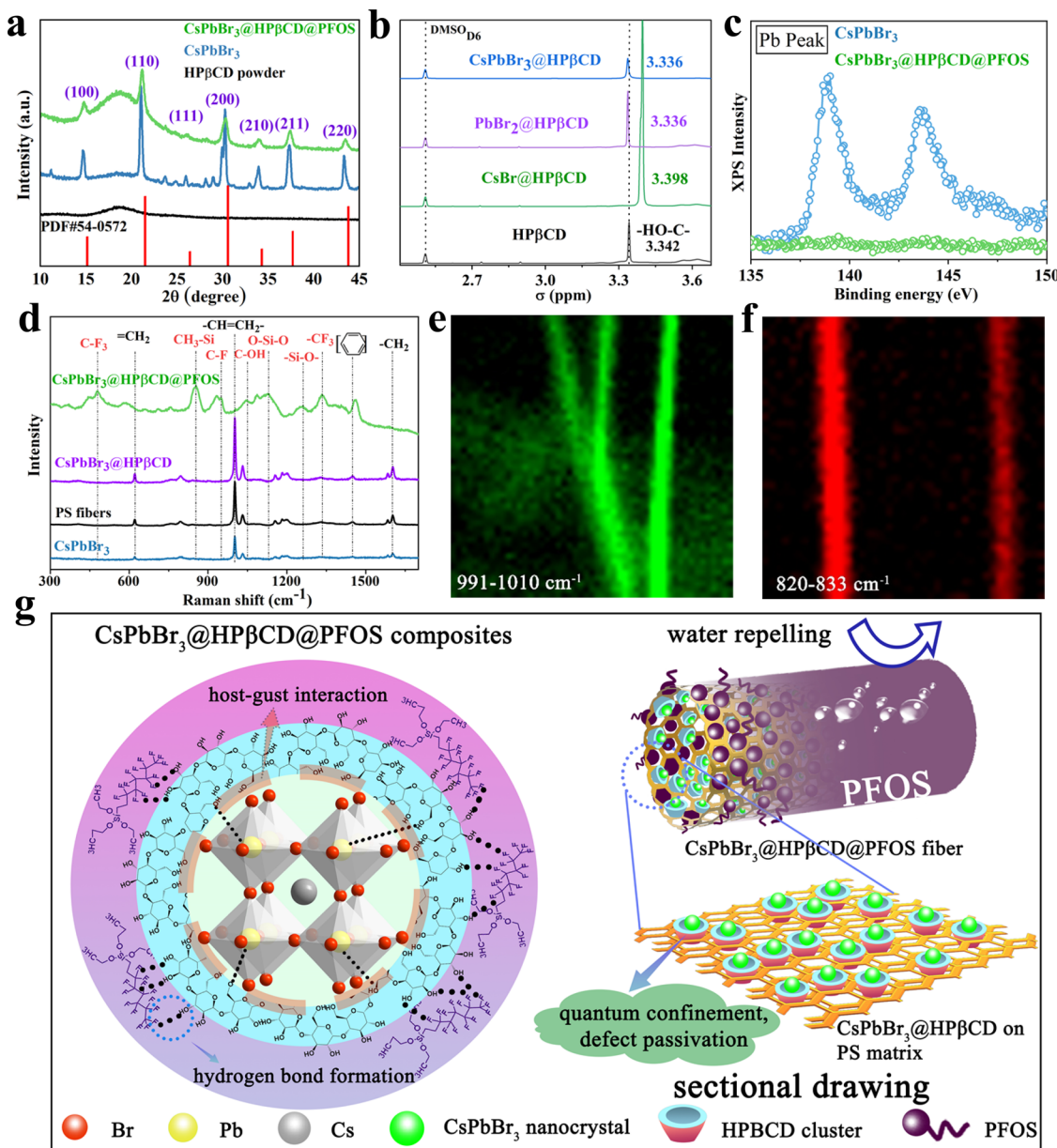


Fig. 2 | Chemical interaction, bonding formation and multifaceted functions of PLTs. **a** XRD patterns of HPβCD power, CsPbBr₃ fibers and CsPbBr₃@HPβCD@PFOS fibers. **b** The ¹H-NMR spectra of HPβCD, CsBr@HPβCD, PbBr₂@HPβCD and CsPbBr₃@HPβCD. **c** XPS spectra of the Pb signal of the CsPbBr₃ fibers and CsPbBr₃@HPβCD@PFOS fibers. **d** Raman spectrum of PS, CsPbBr₃, CsPbBr₃@HPβCD

and CsPbBr₃@HPβCD@PFOS fibers. Raman confocal fluorescence mapping of **(e)** CsPbBr₃ fibers and **(f)** CsPbBr₃@HPβCD@PFOS fibers. **g** Schematic illustration of the chemical interaction of CsPbBr₃@HPβCD@PFOS composites and their multifaceted functions.

waterproofness of the nanofiber composite film. The CsPbBr₃ nanocrystals with the average particle size of 14.24 ± 6.02 nm are uniformly dispersed in the nanofibers (Fig. 1f and Supplementary Fig. 14). The crystalline and amorphous regions of CsPbBr₃@HPβCD@PFOS composite fibers were identified by HRTEM (inset in Fig. 1f). The crystalline regions exhibit distinct and clear lattice fringes (i.e. a distance of 0.356 nm), corresponding to the (111) crystal planes of highly crystalline CsPbBr₃, which reside within the amorphous cyclodextrin and silane surroundings. Note, the CsPbBr₃@HPβCD nanocrystals can be obtained by dissolving the CsPbBr₃@HPβCD fibers in chlorobenzene (CB) solution and then undergoing ultrasonic dispersion for 20 min. The HRTEM image clearly showed the encapsulation of crystalline CsPbBr₃ nanocrystals in amorphous HPβCD matrix (Supplementary Fig. 15). Besides, the elemental mapping of these three kinds of fibers was conducted by using energy dispersive spectroscopy mapping

function in SEM or HRTEM (Supplementary Fig. 16-18), and the corresponding element distribution data was summarized in Supplementary Table 2-4. The results showed that the HPβCD and PFOS play important roles in promoting the uniform distribution of CsPbBr₃ nanocrystals within the polymer skeleton and maintaining the stoichiometric ratio of Cs, Pb and Br (close to 1:1:3).

Chemical interaction mechanism and water-proof property

HPβCD interaction and PFOS encapsulation did not alter the chemical identity of CsPbBr₃, as revealed by X-ray diffraction (XRD) patterns (Fig. 2a) that showed characteristic (100), (110), (111), (200), (210), (211) and (220) planes of cubic CsPbBr₃ for all fibrous films (PDF 54-0752)⁴⁹. Specifically, HPβCD incorporation could facilitate the reaction between the PbBr₂ and CsBr raw materials, diminishing any excess metal halide residues (Supplementary Fig. 19). The slight broadening

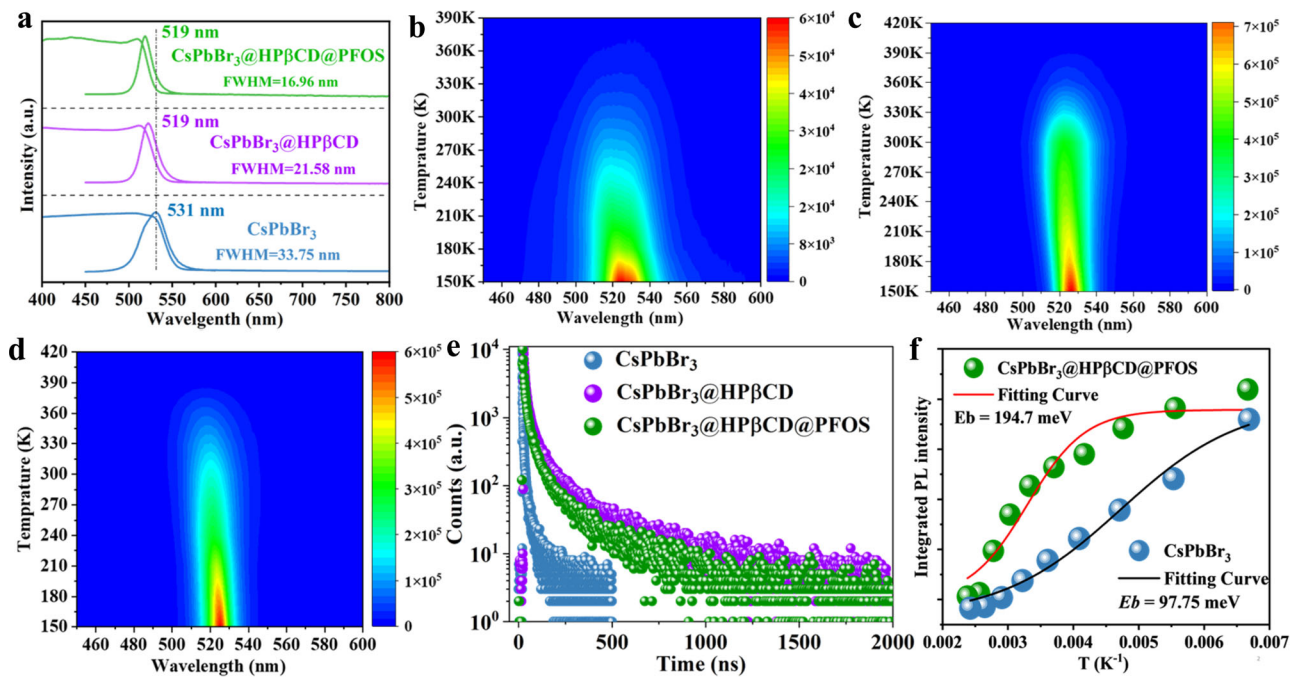


Fig. 3 | The characterization of optical property, temperature-dependent photoluminescence and exciton binding energy of different PLTs. a a UV-visible absorption and PL spectra of CsPbBr₃, CsPbBr₃@HPβCD and CsPbBr₃@HPβCD@PFOS fibers. Temperature-dependent PL mapping of **(b)** CsPbBr₃, **(c)** CsPbBr₃@HPβCD

and **(d)** CsPbBr₃@HPβCD@PFOS fibers. **e** Time-resolved PL decay of CsPbBr₃, CsPbBr₃@HPβCD and CsPbBr₃@HPβCD@PFOS fibers measured at 300 K. **f** Arrhenius plot of integrated PL intensity as a function of the reciprocal temperature (1/T) of CsPbBr₃ and CsPbBr₃@HPβCD@PFOS fibers.

of diffraction peaks in the CsPbBr₃@HPβCD@PFOS fibers can be ascribed to the amorphous characteristic of the HPβCD and PFOS components. ¹H nuclear magnetic resonance (¹H-NMR) spectroscopy provided insights into possible chemical interactions between HPβCD and different species, CsBr, PbBr₂ or CsPbBr₃. The chemical identity of H-3 in the HPβCD molecule is 3.341 ppm, which represents the H atoms located at the hydrophobic inner cavity of HPβCD. After grinding and interaction with CsBr, PbBr₂ or CsPbBr₃ species, the ¹H spectra all shifted, but to different extents. A greater chemical shift was observed for CsBr@HPβCD sample (Fig. 2b), owing to the shorter molecular length of CsBr (~0.35 nm) relative to PbBr₂ (~0.52 nm) (Supplementary Fig. 20), making it much easier to be captured within the HPβCD inner cavity. We also performed XPS to reveal the additional protection efficacy that PFOS has on the CsPbBr₃@HPβCD fibrous film. The control CsPbBr₃ nanofibers exhibited notable signals for the three main elements, Cs, Pb and Br, suggesting that CsPbBr₃ was not fully encapsulated by the polymer matrices (Fig. 2c and Supplementary Fig. 21), which is consistent with the SEM observation (Fig. 1c). In contrast, these elemental signals were all diminished in the CsPbBr₃@HPβCD@PFOS fibrous films, hinting at the full coverage and omnibearing protection of the PFOS layer. Similar characteristic signals have been observed in the Raman spectra of PS, CsPbBr₃ and CsPbBr₃@HPβCD fibrous films, which mostly stem from the Raman shift signals of PS polymer matrices. Again, these PS-related signals disappeared in our CsPbBr₃@HPβCD@PFOS sample (Fig. 2d). The PFOS molecule is embedded with highly polarized C-F bonds and is amphiphilic by nature, meaning it is easy to form strong H-F bonds with numerous -OH groups in HPβCD and expose the superhydrophobic moieties. The hydrogen bonding formation between the PFOS and HPβCD was characterized and analyzed by FTIR (Supplementary Fig. 22) and ¹H-NMR (Supplementary Fig. 23 and Supplementary Table 5). Specifically, the FTIR result showed the broadened signals of -OH, C-F and CF₂/CF₃ groups in the HPβCD@PFOS sample, relative to pristine HPβCD or PFOS sample, which implied the alteration of bonding environment owing to the formation of hydrogen

bonds. The ¹H-NMR spectroscopy further verified the chemical interaction between HPβCD and PFOS. The positions of protons in HPβCD are illustrated in Supplementary Fig. 23, in which the H₂, H₄ and H₆ protons located at the outer surface of HPβCD, and the H₃ and H₅ located at the inner cavity of HPβCD. Upon interacting with PFOS, the resonances of H₂, H₃, H₄, H₅ and H₆ protons in HPβCD molecule all shifted towards high-field positions owing to the formation of hydrogen bonds (Supplementary Table 5). Typically, the chemical shift of H₂, H₄ and H₆ protons is comparatively larger than that of the H₃ and H₅ protons, indicating that the hydrogen bonds were mainly formed between the F atoms of PFOS molecules and the -OH groups of HPβCD outer surface. This result is in good consistency with our demonstrated chemical interaction modes in Fig. 2g (left). With the PFOS protection, a robust water-repelling barrier was established on the surface of PLTs, as is evidenced by the >130° water contact angle (Supplementary Figs. 24 and 25). An optimal content of PFOS (i.e. 150 μL in 1 mL electrospinning ink) ensured the best luminescent property and hydrophobic performance (Supplementary Fig. 26). Raman confocal fluorescence mapping revealed stretching of the -CH=CH₂ (991–1010 cm⁻¹) of PS in the CsPbBr₃ fiber (Fig. 2e), while the CsPbBr₃@HPβCD@PFOS fiber showed only stretching and bending of the -C-F (820–833 cm⁻¹) of PFOS, and without detectable PS-related signals (Fig. 2f)⁵⁰. The host-guest interaction between the CsPbBr₃ nanocrystal and HPβCD clusters, hydrogen bonding formation between HPβCD and PFOS, as well as the multifaceted functions including quantum confinement, multiple defect passivation and water-repellent effect are schematically illustrated in Fig. 2g.

Optical property

Incorporation of HPβCD and PFOS gradually bleached the textiles from yellow to white, and progressively enhanced the luminescent brightness (Supplementary Fig. 27), which can be attributed to effective molecular interaction and encapsulation. Specifically, all of the CsPbBr₃-based fibrous films showed green PL emission, with the strongest PL intensity obtained with CsPbBr₃@HPβCD@PFOS

membranes upon excitation by a 420 nm laser (Supplementary Fig. 28). HP β CD and PFOS modification blue-shifted the PL maxima, which we attribute to the formation of smaller CsPbBr₃ nanocrystals^{16,51}. The modification also led to reduced PL FWHM (Fig. 3a), which was concomitant with an observed enhanced homogeneity for the CsPbBr₃ nanocrystals, namely, uniform in size and well-dispersed in the fibrous matrix (Fig. 1f). The overlap of the absorption band edge and PL emission peak is effectively mitigated by HP β CD and PFOS incorporation, which is desirable to suppress self-absorption and improve luminescence. As a result, the CsPbBr₃@HP β CD@PFOS fibers showed a bright and narrow-band green light emission with high color purity, regardless of excitation wavelength variation from 390 to 440 nm (Supplementary Fig. 29). The enhanced luminescent property and mechanism can be understood through monitoring the carrier dynamics by temperature-dependent PL intensities and lifetimes characterization. Compared with its CsPbBr₃ counterpart, the CsPbBr₃@HP β CD@PFOS fibrous film exhibited a more than fourfold enhancement of radiative recombination rate (K_{rad}) and a 25-fold improvement of PLQY (-50%) (Supplementary Table 6). In addition, the CsPbBr₃@HP β CD and CsPbBr₃@HP β CD@PFOS fibrous films always exhibited stronger PL intensity, narrower FWHM and longer excited-state PL lifetimes when the temperature varied from 150 K to above 390 K (Fig. 3b–e, Supplementary Fig. 30), suggesting significantly improved thermal stability. This result was further confirmed by temperature-dependent XRD testing, which showed that the CsPbBr₃@HP β CD@PFOS fibrous film maintained its crystal structure and composition at high temperature up to 250 °C (Supplementary Fig. 31). During the temperature-dependent PL test, the PL intensities of all the PLTs gradually decreased as the temperature increased, which is a common phenomenon for luminescent materials, especially when the thermal energy is high enough to induce excitons dissociation and facilitate electron-phonon interaction, thus causing significant PL quenching⁴⁸. In addition, one could also notice more obvious blue-shift of PL peak when increasing the temperature from 150 to 300 K, which could be attributed to the fact that, at this low temperature zone, the thermal motion and expansion dominated, which resulted in the bandgap enlargement of semiconducting materials^{52,53}. To better verify the thermal stability of CsPbBr₃@HP β CD@PFOS fibrous film, an additional new set of temperature-dependent PL measurements was conducted by heating the sample from 290 K (near room temperature) to 410 K and then cool down to 290 K. As a result, the PL peak did not blue-shift any more (Supplementary Fig. 32a, b). More interestingly, though one could still notice the PL quenching effect upon heating, the PL intensity was able to recover and became even stronger than before when the sample was subsequently cooled down from 410 K to 290 K (Supplementary Fig. 32c, d). This result suggested our CsPbBr₃@HP β CD@PFOS fibrous film is indeed thermally stable and the PL quenching effect caused by high temperature-induced excitons dissociation is recoverable. For the temperature-dependent PL lifetimes, they also fluctuated with temperature variation. The PL lifetimes were fitted by a triexponential decay function:

$$A(t) = A_1 \exp\left(-\frac{t}{\tau_1}\right) + A_2 \exp\left(-\frac{t}{\tau_2}\right) + A_3 \exp\left(-\frac{t}{\tau_3}\right) \quad (1)$$

At temperatures above 360 K, the CsPbBr₃@HP β CD@PFOS fibrous film showed a remarkably longer PL lifetime (i.e. 90.48 ns) than the other two candidates (i.e. 6.32 ns for CsPbBr₃ and 67.90 ns for CsPbBr₃@HP β CD, Supplementary Fig. 30 and Tables 7–9), further verifying the better thermal stability of the former. This result highlighted the synergistic and beneficial roles of HP β CD inclusion and PFOS encapsulation in mitigating the excitons dissociation and electron-phonon interaction in CsPbBr₃ perovskites under high thermal

stress. The exciton binding energy (E_b) was calculated from the Arrhenius plot, according to the following equation:⁵⁴

$$I(T) = \frac{I_0}{1 + A \exp\left(\frac{E_b}{K_B T}\right)} \quad (2)$$

Where I_0 is the integrated PL intensity at 0 K, K_B is the Boltzmann constant and A is the Arrhenius coefficient. The CsPbBr₃@HP β CD@PFOS composite film had a larger E_b value (194.7 meV) than that of its CsPbBr₃ counterpart (97.75 meV) (Fig. 3f). This suggested a more effective inhibition of exciton dissociation due to the synergic effects of nanoconfinement, encapsulation and special isolation induced by both HP β CD and PFOS modification, thus facilitating the radiative recombination rate and improving the luminescent brightness and PLQYs. Other factors, such as a high surface-to-volume ratio and limited carrier diffusion length of small CsPbBr₃ nanocrystals, suppressed ion migration from quantum dots to quantum dots, well-passivated surface trap-states through HP β CD-assisted host-guest inclusion, and reduced halide deficiency via PFOS-assisted halogen compensation⁵⁵, could contribute together to reduce non-radiative recombination and allow the exciton to recombine via a radiative pathway, thus emitting strong narrow luminescence from isolated crystals.

Stability evaluation

The LHPs are notorious for their intrinsic instability that can occur through light-, thermal- and chemical-induced decomposition, which makes LHPs susceptible to PL quenching^{52,56,57}. We investigated the stability of PLTs in diverse environmental and operational settings, including UV irradiation, ambient storage or water immersion. The CsPbBr₃@HP β CD@PFOS composites textile exhibited outstanding stability for exposure under 24 h continuous UV irradiation (a power density of 120 mW cm⁻²), over 5000 h storage in ambient air (that is, at -20–30 °C and 50–80% relative humidity) and the extrapolated time to drop down to 50% PL (T_{PL50}) is 14,193 h (Supplementary Figs. 33–35). On the one hand, this high ambient stability originates from the effective protection of the encapsulating PFOS layer that enhances the hydrophobicity of the fibrous film and prevents invasion of perovskite by ambient oxygen and water, thus effectively circumventing PL quenching caused by composition decomposition or interaction with external agents in the surrounding environment. On the other hand, the CsPbBr₃ nanocrystals were well-immobilized and stabilized in the polymeric matrix and HP β CD cavities through host-guest inclusion and interaction, and hence the ion diffusion was effectively suppressed, accounting for the substantially extended lifespan under UV light irradiation or thermal stress.

Applications of PLTs

For conventional LHP-based light-emitting devices, nanocrystals with different emission wavelengths are deposited on small-size, rigid substrates, and patterning is very difficult. Electrospinning polymer@perovskite@cyclodextrin@silane composites allow for application in high-resolution patterned displays with bright luminescence and wide color gamut. To demonstrate the versatility of weaving color-tunable PLTs, all-inorganic CsPb(Cl/Br)₃ and CsPb(Br/I)₃-based PLTs were fabricated via a similar composite methodology and electro-spinning process (see the details in the “Methods” of Supplementary Materials). Figure 4a, b shows large-area, patterned perovskite fluorescent displays (10 cm × 10 cm) of different colors (i.e. blue, green and red) that exhibiting excellent uniformity and brightness. It is worth pointing out the red perovskite composites fibrous film also showcased good light stability, which can preserve 73.2% of initial PL intensity after UV light irradiation for 12 h (Supplementary Fig. 36). Through combining commercially available BaMgAl₁₀O₁₇:Eu blue-emitting powder, KSF (K₂SiF₆:Mn⁴⁺) red phosphor,

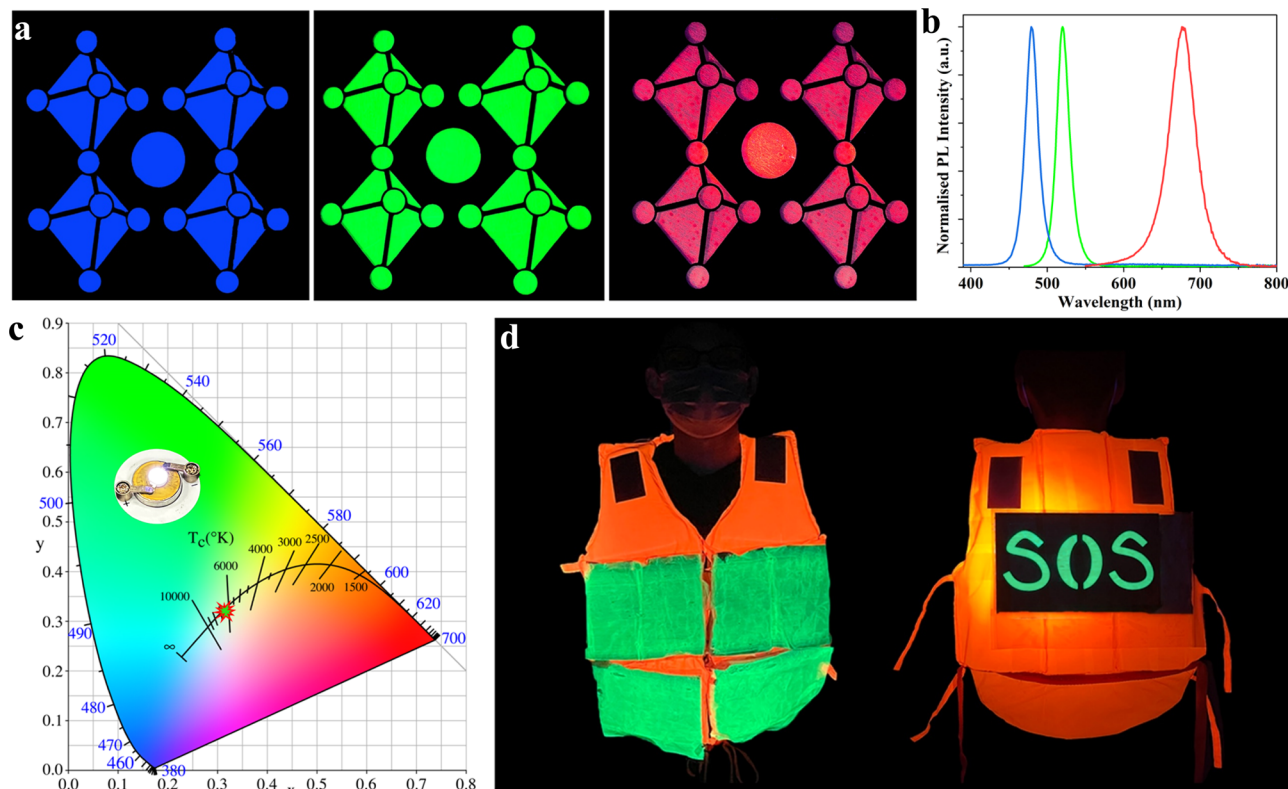


Fig. 4 | Applications of PLTs in patterned display, WLEDs and wearable luminescent clothes. **a** Patterned fluorescent displays ($10\text{ cm} \times 10\text{ cm}$) and **(b)** their corresponding PL spectra of different colors (blue, green and red). **c** The 1931 CIE chromaticity coordinates of white LEDs fabricated with $\text{CsPbBr}_3@\text{HP}\beta\text{CD}@\text{PFOS}$

composites. (The working voltage is 5 V and the driving current is 100 mA.). **d** A demonstration of a life jacket with “SOS” patterned PLT ($10\text{ cm} \times 22\text{ cm}$) sewed on it.

$\text{CsPbBr}_3@\text{HP}\beta\text{CD}@\text{PFOS}$ and a UV chip, our demonstrated monolithic composites can be applied to fabricate white LEDs, showing a color temperature of 6388 K and a color-rendering index of 72.5. The Commission International L'Eclairage (1931CIE) chromaticity coordinates are (0.316, 0.318) (Fig. 4c). Simultaneously, the white LEDs can also be fabricated by stacking all PLTs that emitted blue, green and red light (see Supplementary Fig. 37), which showed a color temperature of 8079 K and a color-rendering index of 67.5. The Commission International L'Eclairage (1931CIE) chromaticity coordinates are (0.2822, 0.3421). Given that the woven PLTs are flexible, lightweight, durable, and have fascinating luminescent properties and robust mechanical strength (Supplementary Movie # 2), we envision a great potential for them to be used as wearable luminescent clothes in marine rescue or night work safety. As a proof-of-concept, we demonstrated a life jacket with a large-area ($10\text{ cm} \times 22\text{ cm}$) “SOS” pattern and other sheets sewed on it (Fig. 4d), which could send a macroscopic SOS signal when people are encountering danger in a marine environment.

Considering that the marine environment and real circumstances are complex and dynamic (e.g. water flow, pH values and depth), we purposely investigated the acid/base resistance of PLTs and evaluated their safety and reliability in terms of sequestering toxic components. The $\text{CsPbBr}_3@\text{HP}\beta\text{CD}@\text{PFOS}$ textile preserved ~63–73% of PLQY when immersed in water of pH = 1.2 (PLQY = 31.4%) and pH = 12.8 (PLQY = 36.3%) for 24 h (Supplementary Figs. 38 and 39). We also evaluated the tolerance of PLTs upon high pressure extrusion (related to the seabed depth), when a rescuer dives deep into the sea. When pressure increases to 30 MPa (equivalent to 3000 meters in depth), the PLT still preserved 38% of its initial PL intensity, with a slightly enlarged FWHM (Fig. 5a). Our demonstrated $\text{CsPbBr}_3@\text{HP}\beta\text{CD}@\text{PFOS}$ -based PLT showed strong water resistance, which preserved more than 85% PL

intensity even after 3260 h immersion (Fig. 5b), and the extrapolated T_{PL50} is ~12,189 h (Supplementary Fig. 35). A home-made apparatus was used to simulate the real conditions of PLTs under dynamic seawater scour at a fast flow rate of 570 mL min⁻¹, during which the PLT could continuously emit green light upon excitation (Fig. 5c and Supplementary Movie # 3). As revealed by inductively coupled plasma-mass spectrometer (ICP-MS) measurement, a negligible Pb²⁺ concentration of 3.94 ppt (Fig. 5d) was detected after dynamic scouring for 3300 h, which is 8 orders of magnitude lower than the regulated Pb content in drinking-water (<0.01 ppm) according to the World Health Organization guidelines. This excellent capability of inhibiting Pb ions leakage can be ascribed to the in-situ encapsulation and effective chemisorption of heavy metal ions by HPβCD cluster. In addition, the polymer matrices and outer PFOS physical barrier can effectively fix Pb²⁺ ions on the resin/nanosilane composites. In this case, the Pb²⁺ was not easily leached out even when scoured by high-flow rate water, making our demonstrated PLTs environmentally viable and safe. To the best of our knowledge, our demonstrated $\text{CsPbBr}_3@\text{HP}\beta\text{CD}@\text{PFOS}$ composites-based PLTs exhibit exceptional luminescent properties and stability, which offered substantial advantages over other reported state-of-the-art analogues (Supplementary Table 10).

Discussion

We present a new type of large-area, functional luminescent textiles fabricated by electrospinning of polymer@perovskite@cyclodextrin@silane composites. The PLTs are waterproof and durable in a variety of harsh conditions, offering substantial advantages (i.e. high PLQY, high color purity and good stability) over other LHP composites reported to date. Our demonstrated approach rationally combined the strategies of host-guest chemical interaction, inclusion-like encapsulation and physical

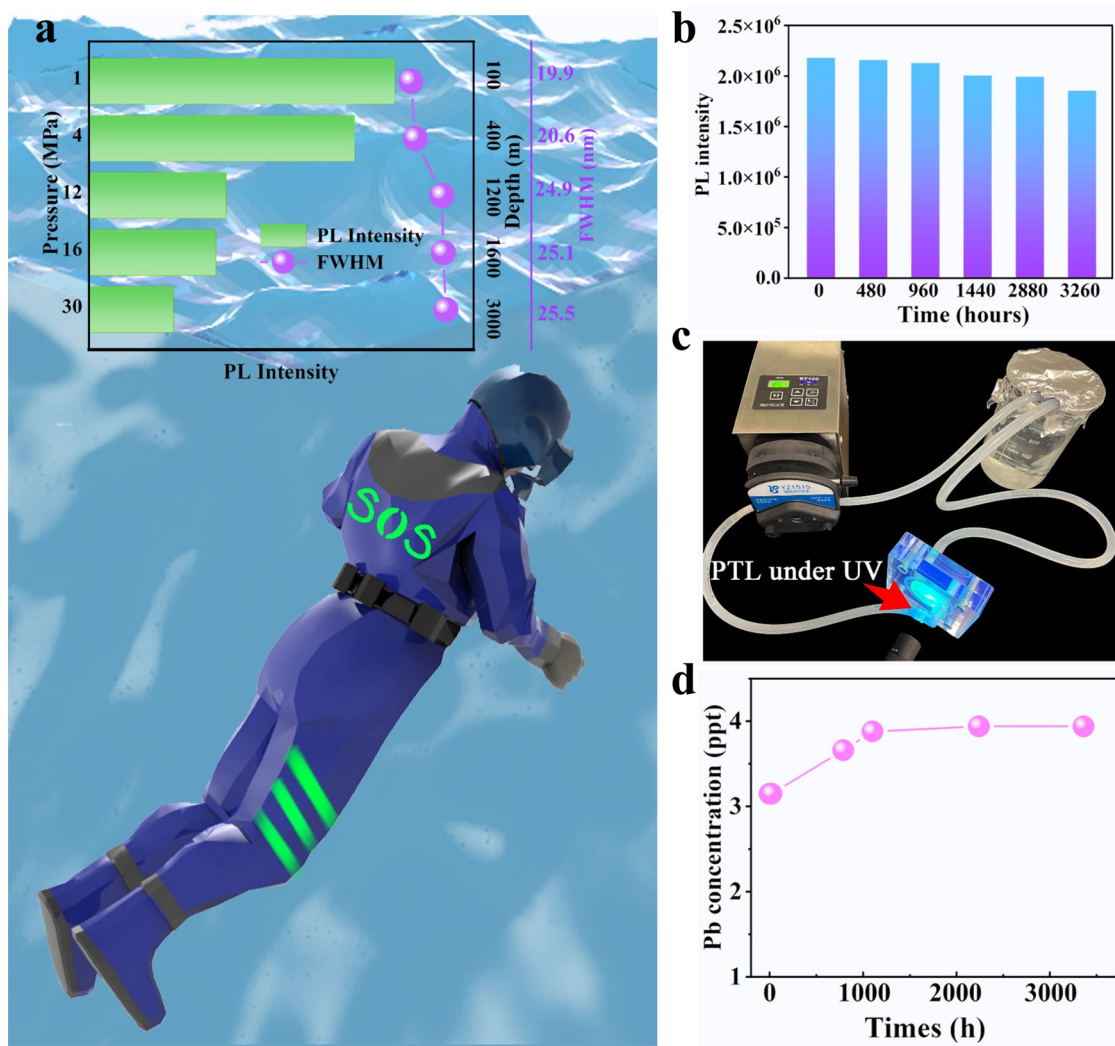


Fig. 5 | Demonstration of PLT in marine rescue. **a** The evolution of PL intensity and FWHM of $\text{CsPbBr}_3@\text{HPbCD}@PFOS$ -based PLTs as a function of pressure and depth, and the schematic image of an “SOS” signal patterned on the life jacket made by $\text{CsPbBr}_3@\text{HPbCD}@PFOS$ fiber. **b** The evolution of PL intensity of

$\text{CsPbBr}_3@\text{HPbCD}@PFOS$ -based PLTs during 3260 h of water immersion. **c** The setup to simulate the real conditions of PLTs under dynamic seawater scour. **d** A trace of leaked Pb ions concentrations after extended scouring time.

blocking, and smartly integrated them into a single fabrication process, which remarkably advances the fabrication of perovskite materials and devices with high throughput and high scalability in a cost-effective manner. We show that such a flexible, stable, durable and safe luminescent textile can be used in a variety of optoelectronic applications, such as high-resolution patterned displays, white LEDs and wearable fluorescence products for marine rescue. This work provides a new perspective for fabricating high-performance perovskite luminescent materials with low-cost advantage and safety warranty. We anticipate that this finding will promote the large-scale production and practical applications of luminescent textiles for next-generation smart and wearable optoelectronics.

Methods

Materials

Cesium bromide (CsBr), Cesium chloride (CsCl), lead chloride (PbCl_2) and Iodine Cesium (CsI_2) were purchased from Xi'an Polymer Light Technology Corp. Lead bromide (PbBr_2 , 99.9%) and lead iodine (PbI_2) were purchased from Aladdin. The N,N-dimethylformamide (DMF, AR), n-hexane and dimethyl sulfoxide (DMSO) were purchased from Shanghai Yinli Science and Technology Co., Ltd. Perfluorooctyltriethoxysilane

(PFOS) was purchased from Heowns Industrial Corporation. Hydroxypropyl- β -cyclodextrin ($\text{HP}\beta\text{CD}$), polystyrene (PS) and deuterated dimethylsulfoxide (DMSO-d_6) were purchased from Shanghai Macklin Biochemical Co., Ltd. All chemicals were used as received without further purification. The commercial $\text{BaMgAl}_{10}\text{O}_{17}:\text{Eu}$ blue-emitted powder and $\text{K}_2\text{SiF}_6:\text{Mn}^{4+}$ (KSF) red phosphors were purchased from Shenzhen looking long technology Co., LTD.

Fabrication of large-area PLTs (15 cm × 25 cm)

Various combination of perovskite powders, 0.0212 g CsBr and 0.0367 g PbBr_2 (for green-emitting CsPbBr_3), 0.0168 g CsCl , 0.0177 g PbCl_2 and 0.005 g CsBr (for blue-emitting $\text{CsPb}(\text{Cl}/\text{Br})_3$), or 0.002 g CsBr , 0.026 g CsI and 0.036 g PbI_2 (for red-emitting $\text{CsPb}(\text{Br}/\text{I})_3$) were ground with 0.013 g $\text{HP}\beta\text{CD}$ for 1 h to obtain perovskite@ $\text{HP}\beta\text{CD}$ composite powders. Next, the perovskite@ $\text{HP}\beta\text{CD}$ powder, 150 μl PFOS and 0.17 g PS were mixed together in 1 ml DMF/DMSO mixed solvent (7:3 volume ratio) to prepare the electrospinning ink (Note: this method can be scaled up.). The ink was poured into a syringe (1 mL) fitted with a metallic needle (inner diameter of 0.45 mm). During the process of electrospinning, the syringe was positioned horizontally on a syringe pump, the electrode at the high voltage power supply was clamped to the metal needle tip and ground to an

aluminum collector wrapped with aluminum foil (the supporting substrate of PLTs). An applied voltage of 10 kV, a tip-to-collector distance of 10 cm, and a solution flow rate of 1.0 mL h⁻¹ was set for weaving the PLTs. The electrospinning apparatus (E02, Foshan Qingzi Precision Measurement and Control Technology Co., Ltd) was enclosed in a Plexiglass box and the electrospinning was carried out at 22–26 °C under 50–60% relative humidity.

WLEDs fabrication

In total, 5.8 mg of CsPbBr₃@HPβCD@PFOS fibers were mixed with 5 mg of BaMgAl₁₀O₁₇:Eu blue-emitted powder and 15 mg of commercial K₂SIF₆:Mn⁴⁺ (KSF) red phosphors. The mixed phosphors were applied to 380 nm purple-emitting InGaN chips (Shenzhen looking long technology co., LTD.) to obtain WLEDs, which operated at a working voltage of 5 V and a current of 10 mA.

Setup of the dynamic seawater scouring apparatus

A setup of a home-made dynamic seawater scouring apparatus was composed of a peristaltic pump, a 1000 ml beaker and film holder. The CsPbBr₃@HPβCD@PFOS PLT was set in the film holder under dynamic water scouring, which continuously emitted green light upon UV light irradiation.

Characterization

The UV-vis absorption (Shimadzu) equipped with an integrating sphere was used to characterize the absorption of CsPbBr₃, CsPbBr₃@HPβCD and CsPbBr₃@HPβCD@PFOS fibers. The morphological features of the samples were characterized using a cold-field emission scanning electron microscope (SEM, Regulus 8230), equipped with a flat-inserted energy spectrum (spatial resolution 10 nm) and YAG back-scattered electron detector (secondary electron mode (SE) and backscattered electron image (BSE) mode can be chosen). The microstructures of the fibers were examined using a transmission electron microscope (TEM, FEI Tecnai G2 F30, 300 kV.) and spherical aberration-corrected transmission electron microscope (JEM-ARM200P, 200 kV) operating at an accelerating voltage of 200 kV. The bright field and photoluminescence (PL) images of PLTs were characterized by a fluorescence microscope (Leica, LSM880) and a confocal laser fluorescence microscope (Zeiss, LSM 710 NLO). The temperature-dependent XRD spectra of the samples were measured on an X-ray diffractometer (Bruker D8 ADVANCE). The 2θ range was 5° to 45°, with a step size of 0.02° and a step rate of 10 s, and the temperature range was from 30 to 250 °C. Room-temperature XRD analysis was also collected (Rigaku D-MAX 2200 VPC). X-ray photoelectron spectroscopy (XPS, ESCALAB 250, Thermo Fisher Scientific) was used to investigate the chemical identity of the samples. The sample surface chemistry was probed with mono Al Kα (1486.6 eV) at 150 W (12 kV, 6 mA). The absolute PLQY values were assessed by a C 9920-02 absolute PL quantum yield measurement system (Hamamatsu Spectral Photometry C9920-02G.). The optical performance of the WLEDs was measured by an OSHP 350 M spectrophotometer with a 50 cm integrating sphere. An Edinburgh Instruments Ltd FLS1000 was used to test steady-state PL, time-resolved PL decay (TRPL), temperature-dependent PL mapping, and temperature-dependent TRPL. The sample was cooled to 150 K firstly, and gradually increased by 30 K until reached 390 K and above. Each temperature point was stable for 10 min. Raman spectra were measured with a Renishaw Raman microscope and spectrometer. The spectral range was adjusted from 100 to 3100 cm⁻¹, and the spectral resolution was 1 cm⁻¹. All samples were excited with a 785 nm laser beam. Ten cycles of data collection were implemented to reduce the effect of background noise caused by strong fluorescence. The proton nuclear magnetic resonance (¹H-NMR) characterization was performed on an AVANCE NEO 600 M (Bruker), with DMSO-d₆ (Merck) used as the reference NMR solvent. The molecular

lengths of CsBr and PbBr₂ were calculated by Chemdraw 19.0. published in 2019.

Reporting summary

Further information on research design is available in the Nature Portfolio Reporting Summary linked to this article.

Data availability

The source data generated in this study are provided in the 'Source Data' file. Source data are provided with this paper.

References

1. Cao, Y. et al. Perovskite light-emitting diodes based on spontaneously formed submicrometre-scale structures. *Nature* **562**, 249–253 (2018).
2. Chiba, T. et al. Anion-exchange red perovskite quantum dots with ammonium iodine salts for highly efficient light-emitting devices. *Nat. Photon.* **12**, 681–687 (2018).
3. Dong, Q. et al. Interpenetrating interfaces for efficient perovskite solar cells with high operational stability and mechanical robustness. *Nat. Commun.* **12**, 973 (2021).
4. Gong, X. et al. Highly efficient quantum dot near-infrared light-emitting diodes. *Nat. Photon.* **10**, 253–257 (2016).
5. Kim, Y.-H. et al. Comprehensive defect suppression in perovskite nanocrystals for high-efficiency light-emitting diodes. *Nat. Photon.* **15**, 148–155 (2021).
6. Kovalenko, M. V., Protesescu, L. & Bodnarchuk, M. I. Properties and potential optoelectronic applications of lead halide perovskite nanocrystals. *Science* **358**, 745–750 (2017).
7. Liu, X.-K. et al. Metal halide perovskites for light-emitting diodes. *Nat. Mater.* **20**, 10–21 (2021).
8. Liu, Y. et al. Efficient blue light-emitting diodes based on quantum-confined bromide perovskite nanostructures. *Nat. Photon.* **13**, 760–764 (2019).
9. Wang, N. et al. Perovskite light-emitting diodes based on solution-processed self-organized multiple quantum wells. *Nat. Photon.* **10**, 699–704 (2016).
10. Quan, L. N., García de Arquer, F. P., Sabatini, R. P. & Sargent, E. H. Perovskites for light emission. *Adv. Mater.* **30**, 1801996 (2018).
11. Sun, C. et al. High-performance large-area quasi-2D perovskite light-emitting diodes. *Nat. Commun.* **12**, 2207 (2021).
12. Xu, W. et al. Rational molecular passivation for high-performance perovskite light-emitting diodes. *Nat. Photon.* **13**, 418–424 (2019).
13. Zhao, B. et al. High-efficiency perovskite-polymer bulk heterostructure light-emitting diodes. *Nat. Photon.* **12**, 783–789 (2018).
14. Hou, J. et al. Liquid-phase sintering of lead halide perovskites and metal-organic framework glasses. *Science* **374**, 621–625 (2021).
15. Sun, K. et al. Three-dimensional direct lithography of stable perovskite nanocrystals in glass. *Science* **375**, 307–310 (2022).
16. Wang, H.-C. et al. Mesoporous silica particles integrated with all-inorganic CsPbBr₃ perovskite quantum-Dot nanocomposites (MP-PQDs) with high Stability and wide color gamut used for backlight display. *Angew. Chem. Int. Ed.* **55**, 7924–7929 (2016).
17. Sun, C. et al. Efficient and stable white LEDs with silica-coated inorganic perovskite quantum dots. *Adv. Mater.* **28**, 10088–10094 (2016).
18. Wang, S. et al. Original core-shell structure of cubic CsPbBr₃@amorphous CsPbBr_x perovskite quantum dots with a high blue photoluminescence quantum yield of over 80%. *ACS Energy Lett.* **3**, 245–251 (2018).
19. Shi, X. et al. Large-area display textiles integrated with functional systems. *Nature* **591**, 240–245 (2021).
20. Du, P. et al. Efficient and large-area all vacuum-deposited perovskite light-emitting diodes via spatial confinement. *Nat. Commun.* **12**, 4751 (2021).

21. Duan, Y. et al. Meeting high stability and efficiency in hybrid light-emitting diodes based on $\text{SiO}_2/\text{ZrO}_2$ coated CsPbBr_3 perovskite nanocrystals. *Adv. Funct. Mater.* **30**, 2005401 (2020).
22. Chu, S. et al. Large-area and efficient perovskite light-emitting diodes via low-temperature blade-coating. *Nat. Commun.* **12**, 147 (2021).
23. Zhang, C. et al. Conversion of invisible metal-organic frameworks to luminescent perovskite nanocrystals for confidential information encryption and decryption. *Nat. Commun.* **8**, 1138 (2017).
24. Lian, H. et al. Highly thermotolerant metal halide perovskite solids. *Adv. Mater.* **32**, 2002495 (2020).
25. Wei, Y. et al. Enhancing the stability of perovskite quantum dots by encapsulation in crosslinked polystyrene beads via a swelling-shrinking strategy toward superior water resistance. *Adv. Funct. Mater.* **27**, 1703535 (2017).
26. Chen, J. et al. Emerging perovskite quantum dot solar cells: feasible approaches to boost performance. *Energy Environ. Sci.* **14**, 224–261 (2021).
27. Swarnkar, A. et al. Quantum dot-induced phase stabilization of α - CsPbI_3 perovskite for high-efficiency photovoltaics. *Science* **354**, 92–95 (2016).
28. Protesescu, L. et al. Nanocrystals of cesium lead halide perovskites (CsPbX_3 , X = Cl, Br, and I): novel optoelectronic materials showing bright emission with wide color gamut. *Nano Lett.* **15**, 3692–3696 (2015).
29. Tao, W. et al. Momentarily trapped exciton polaron in two-dimensional lead halide perovskites. *Nat. Commun.* **12**, 1400 (2021).
30. Wang, Q. et al. Efficient sky-blue perovskite light-emitting diodes via photoluminescence enhancement. *Nat. Commun.* **10**, 5633 (2019).
31. Ahmed, G. H. et al. Successes and challenges of core/shell lead halide perovskite nanocrystals. *ACS Energy Lett.* **6**, 1340–1357 (2021).
32. Zhou, Y. et al. Perovskite anion exchange: a microdynamics model and a polar adsorption strategy for precise control of luminescence color. *Adv. Funct. Mater.* **31**, 2106871 (2021).
33. Liu, Y. et al. Tough, stable and self-healing luminescent perovskite-polymer matrix applicable to all harsh aquatic environments. *Nat. Commun.* **13**, 1338 (2022).
34. Yu, B. et al. Water-stable CsPbBr_3 perovskite quantum-dot luminous fibers fabricated by centrifugal spinning for dual white light illumination and communication. *Photon. Res.* **9**, 1559–1568 (2021).
35. Lu, X. et al. Fiber-spinning-chemistry method toward in situ generation of highly stable halide perovskite nanocrystals. *Adv. Sci.* **6**, 1901694 (2019).
36. Hai, J. et al. Designing of blue, green, and red CsPbX_3 perovskite-codoped flexible films with water resistant property and elimination of anion-exchange for tunable white light emission. *Chem. Commun.* **53**, 5400–5403 (2017).
37. Cheng, R. et al. Fibrous nanoreactors from microfluidic blow spinning for mass production of highly stable ligand-free perovskite quantum dots. *Angew. Chem. Int. Ed.* **61**, e202204371 (2022).
38. Li, J.-J. et al. Stable and large-scale organic-inorganic halide perovskite nanocrystal/polymer nanofiber films prepared via a green in situ fiber spinning chemistry method. *Nanoscale* **14**, 11998–12006 (2022).
39. Zhang, Y. et al. Homogeneous freestanding luminescent perovskite organogel with superior water stability. *Adv. Mater.* **31**, 1902928 (2019).
40. Liao, H. et al. A general strategy for in situ growth of all-inorganic CsPbX_3 (X = Br, I, and Cl) perovskite nanocrystals in polymer fibers toward significantly enhanced water/thermal stabilities. *Adv. Opt. Mater.* **6**, 1800346 (2018).
41. Uyar, T. et al. Functional electrospun polystyrene nanofibers incorporating α -, β -, and γ -Cyclodextrins: comparison of molecular filter performance. *ACS Nano* **4**, 5121–5130 (2010).
42. Alsbaiee, A. et al. Rapid removal of organic micropollutants from water by a porous β -cyclodextrin polymer. *Nature* **529**, 190–194 (2016).
43. Wu, W.-Q. et al. Spontaneous surface/interface ligand-anchored functionalization for extremely high fill factor over 86% in perovskite solar cells. *Nano Energy* **75**, 104929 (2020).
44. Zhao, F. et al. EDTA-cross-linked β -cyclodextrin: an environmentally friendly bifunctional adsorbent for simultaneous adsorption of metals and cationic dyes. *Environ. Sci. Technol.* **49**, 10570–10580 (2015).
45. Ravi, V. K. et al. Orcid origin of the substitution mechanism for the binding of organic ligands on the surface of CsPbBr_3 perovskite nanocubes. *J. Phys. Chem. Lett.* **8**, 4988–4994 (2017).
46. Levitt, M. H. Spin dynamics: basics of nuclear magnetic resonance. (Wiley Press, New York, 2001).
47. Hens, Z. & Martins, J. C. A solution NMR toolbox for characterizing the surface chemistry of colloidal nanocrystals. *Chem. Mater.* **25**, 1211–1221 (2013).
48. Shamsi, J. et al. Metal halide perovskite nanocrystals: synthesis, post-synthesis modifications, and their optical properties. *Chem. Rev.* **119**, 3296–3348 (2019).
49. Zhou, S., Tang, R. & Yin, L. Slow-photon-effect-induced photoelectrical-conversion efficiency enhancement for carbon-quantum-dot-sensitized inorganic CsPbBr_3 inverse opal perovskite solar cells. *Adv. Mater.* **29**, 1703682 (2017).
50. Smith, E. & Dent, G. Modern Raman Spectroscopy-a Practical Approach. (Wiley Press, New York, 2004).
51. Zhang, D. et al. Large-scale planar and spherical light-emitting diodes based on arrays of perovskite quantum wires. *Nat. Photon.* **16**, 284–290 (2022).
52. Zhang, D. et al. Solution-phase synthesis of cesium lead halide perovskite nanowires. *J. Am. Chem. Soc.* **137**, 9230–9233 (2015).
53. Wei, K. et al. Temperature-dependent excitonic photoluminescence excited by two-photon absorption in perovskite CsPbBr_3 quantum dots. *Opt. Lett.* **41**, 3821–3824 (2016).
54. Nikitine, S. The Philosophical Magazine: a Journal of Theoretical Experimental and Applied Physics, **4**, 1-31 (Taylor & Francis Press, London, 1959).
55. Wu, W.-Q. et al. Reducing surface halide deficiency for efficient and stable iodide-based perovskite solar cells. *J. Am. Chem. Soc.* **142**, 3989–3996 (2020).
56. Wang, Y.-K. et al. Chelating-agent-assisted control of CsPbBr_3 quantum well growth enables stable blue perovskite emitters. *Nat. Commun.* **11**, 3674 (2020).
57. Yang, D. et al. Facet-induced coordination competition for highly ordered CsPbBr_3 nanoplatelets with strong polarized emission. *Nano Res.* **15**, 502–509 (2022).

Acknowledgements

We acknowledge financial support from the National Natural Science Foundation of China (22005355), the Guangdong Basic and Applied Basic Research Foundation (2022A1515010282) and the Fundamental Research Funds for the Central Universities, Sun Yat-sen University (22qntd2305). L. Wang acknowledges the financial support from ARC through its Discovery program.

Author contributions

W.Q.W., T.T. and L.W. designed the experiment. T.T. and M.Y. carried out the experimental study on luminous textile fabrication and characterization. Y.F., S.Z. and Y.C. analyzed the data. W.Q.W., T.T. and L.W. wrote the manuscript. All the authors reviewed the manuscript.

Competing interests

The authors declare no competing interests.

Additional information

Supplementary information The online version contains supplementary material available at
<https://doi.org/10.1038/s41467-023-35830-8>.

Correspondence and requests for materials should be addressed to Lianzhou Wang or Wu-Qiang Wu.

Peer review information : *Nature Communications* thanks Xin-Rui Ding and the other, anonymous, reviewers for their contribution to the peer review of this work.

Reprints and permissions information is available at
<http://www.nature.com/reprints>

Publisher's note Springer Nature remains neutral with regard to jurisdictional claims in published maps and institutional affiliations.

Open Access This article is licensed under a Creative Commons Attribution 4.0 International License, which permits use, sharing, adaptation, distribution and reproduction in any medium or format, as long as you give appropriate credit to the original author(s) and the source, provide a link to the Creative Commons license, and indicate if changes were made. The images or other third party material in this article are included in the article's Creative Commons license, unless indicated otherwise in a credit line to the material. If material is not included in the article's Creative Commons license and your intended use is not permitted by statutory regulation or exceeds the permitted use, you will need to obtain permission directly from the copyright holder. To view a copy of this license, visit <http://creativecommons.org/licenses/by/4.0/>.

© The Author(s) 2023